Applied Surface Science 696 (2025) 162997

Contents lists available at ScienceDirect

Applied Surface Science

journal homepage: www.elsevier.com/locate/apsusc

Full Length Article

Angle-resolved ellipsometric analysis of polishing-induced subsurface damages in calcium fluoride crystals for ultra-precision manufacturing

Tianqi Jia [a], Jian Wang [a,*], Lihua Peng [a], Wei Guo [a], Wenjuan Sun [b], Shiyuan Liu [a]

[a] State Key Lab of Intelligent Manufacturing Equipment and Technology, Huazhong University of Science and Technology, Wuhan 40074, China
[b] Department of Mechanical Engineering, KU Leuven, Celestijnenlaan 300, Leuven 3001, Belgium

ARTICLE INFO

Keywords:
Angle-resolved ellipsometry
Subsurface damages
Finite-difference time-domain
Optical crystals
Non-destructive test

ABSTRACT

Calcium fluoride (CaF_2), renowned for its exceptional optical and mechanical properties, is a critical material in advanced semiconductor and optical manufacturing. However, tribological processes such as polishing introduce subsurface damages (SSDs), including micro-cracks and lattice dislocation, which degrade functional performance and reduce service life. This study presents a novel, nondestructive method for SSD inspection using single-shot angle-resolved ellipsometric spectra (ARES) acquisition and analysis. The effects of SSD layer thickness and surface roughness on ARES are systematically evaluated through the effective medium approximation. Finite-difference time-domain simulations demonstrate the high sensitivity of Ψ-ARES (p-/s- amplitude ratio) to nanoscale SSD variations. An ARES measurement system employing back-focal-plane imaging was developed to validate the approach on CaF_2 samples subjected to varying polishing conditions. The results showed good agreement with that of atomic force microscopy, white light interferometry and transmission electron microscopy. This work establishes angle-resolved ellipsometry as a powerful tool for nondestructive subsurface damage evaluation, enabling improved polishing processes and enhanced performance of ultra-precision manufacturing.

1. Introduction

Calcium fluoride (CaF_2), renowned for its exceptional optical and physical properties, is widely used as a critical window material in deep ultraviolet lithography and the aerospace industry. These properties include high optical isotropy, superior transmission, temperature resistance, and corrosion resistance [1–5]. High surface quality, encompassing well controlled surface roughness (SR) and subsurface damage (SSD) [6–8], is essential in these industries. Among these, SSD is a crucial indicator of surface quality, as it significantly impacts the functional performance and service life of lithography systems and semiconductor devices [9–11]. SSD forms during mechanical processing due to stress and chemical reactions, manifesting in internal fractures, amorphous structures, dislocations, layering, lattice distortions, and residual stress [12–14]. Accurate and efficient characterization of SSD is critical for achieving the required surface quality in optical crystals.

1.1. Current SSD characterization methods

Current SSD characterization methods are often destructive, even when partially contactless optical tools are employed. For example, white light interferometry (WLI) can nondestructively measure SR but becomes destructive for SSD inspection, requiring critical sample preprocessing, such as surface etching. Chu et al. [15] used WLI to analyze SSD morphology in molten silicon by etching surfaces, establishing a relationship between SSD and resonator quality factor. Similarly, Guo et al. [16] employed transmission electron microscopy (TEM) to investigate the tough-brittle transformation mechanism in CaF_2 micro-cutting processes. Currently, TEM is a typical method for characterizing SSD [17–19]. However, destructive methods reduce reliability and efficiency because sample surface layers must be destructed prior to measurement.

Optical coherence tomography (OCT) and scanning acoustic microscopy (SAM) are typical nondestructive techniques for SSD characterization [20,21]. However, OCT struggles to achieve the nanoscale resolution required for precise SSD measurements [20]. SAM is constrained by environmental requirements due to its reliance on acoustic coupling via a water medium [22]. Emerging optical methods, including Raman spectroscopy, X-ray diffraction, and ellipsometry, have been proposed for nondestructive surface quality evaluation. Raman spectroscopy, for instance, provides information on lattice vibrations influenced by microstructure changes and residual stress [23–25]. Zhou et al.

* Corresponding author.
E-mail address: jianwang@hust.edu.cn (J. Wang).

https://doi.org/10.1016/j.apsusc.2025.162997
Received 25 December 2024; Received in revised form 23 February 2025; Accepted 14 March 2025
Available online 16 March 2025

Nomenclature

Δ	Phase retardance
ε	Dielectric constant
λ	Wavelength
Ψ	Amplitude ratio
σ	Root-mean-square surface roughness
θ	Incident angle
θ_B	Brewster angle
θ_q	Quasi-Brewster angle
AFM	Atomic force microscope
ARE	Angle-resolved ellipsometry
ARES	Angle-resolved ellipsometric spectra
BFP	Back-focal plane
CaF_2	Calcium fluoride
d_1	Surface roughness layer thickness
d_2	Subsurface damage layer thickness
d_{EMA}	EMA equivalent thickness
EMA	Effective medium approximation
FDTD	Finite-difference time-domain
G_q	Gradient angle of θ_q in Δ-ARES
h	Average layer thickness in EMA
n	Refractive index
NA	Numerical aperture
OCT	Optical coherence tomography
q-BAT	Quasi-Brewster angle technique
r	BFP radius
S_B	Angular shift of θ_B in Ψ-ARES
S_q	Angular shift of θ_q in Δ-ARES
SR	Surface roughness
SSD	Subsurface damage
TEM	Transmission electron microscopy
VASE	Variable angle spectroscopic ellipsometry
WLI	White light interferometry

[26] demonstrated the plastic deformation mechanism of gadolinium gallium garnet during atomic-scale grinding using Raman spectroscopy. However, conventional Raman signals are weak for nanoscale SR layers, and tip-based Raman spectroscopy, while effective for film thicknesses of 30 nm, incurs high costs [27]. X-ray diffraction has been used to evaluate SSD in CaF_2 grinding processes, correlating micro-cracks with diffraction curve patterns [28]. Yet, complex equipment and sample limitations (e.g., powders) hinder its broad application [25]. These limitations underscore the urgent need to develop new nondestructive and high-precision SSD characterization methods.

1.2. Ellipsometry combined with advanced modeling

With its sub-nanometer sensitivity, Ellipsometry has recently emerged as a promising tool for SSD inspection. Ellipsometry can infer SSD depth through advanced optical modeling, e.g., effective medium approximation (EMA) by measuring surface layer thickness and refractive index. Wang et al. [29] introduced the quasi-Brewster angle technique (q-BAT) to measure SR and SSD depths in optical crystals simultaneously. Yao et al. [30,31] applied q-BAT with variable angle spectroscopic ellipsometry to evaluate the surface quality of polished Lu_2O_3 and yttrium aluminum garnet crystals. These studies emphasized the significance of angular spectra of the phase retardance (Δ) between *p*- and *s*- polarized light by simply correlating the angular shift and spectral curve slope at $\Delta = 90^{\circ}$ to SSD and SR separately. However, q-BAT often leads to confusion, as it ignores the angular shifts caused by SR, resulting in reduced accuracy. In addition, the theoretical foundation of q-BAT has yet to be understood appropriately.

Finite-difference time-domain (FDTD) simulations have validated EMA's reliability. For example, Yu et al. [32] analyzed SiO_2 thin films using FDTD, and established a functional relationship of EMA equivalent thickness (d_{EMA}) in terms of root-mean-square SR (σ) and average layer height (h): $d_{EMA} = \sigma + 0.8h$. Huang et al. [33] demonstrated that EMA accuracy for SR evaluation improves as the ratio of σ to light wavelength (λ) decreases. Fung et al. [34] explored EMA's applicability for randomly rough surfaces regarding σ/λ under normal incidence light and highlighted the need for studies under oblique incidence conditions. While these studies focus on SR evaluation, research on SSD characterization using EMA remains limited.

1.3. Challenges and contribution

The following key challenges remain unresolved: 1) The theoretical validity of q-BAT for SSD evaluation needs further examination, particularly in separating SR and SSD contributions. The inability to distinguish and quantify SSD and SR layer thicknesses using Δ angle-resolved ellipsometric spectra (Δ–ARES) compromises accuracy. 2) Existing ellipsometry systems rely on variable-angle scanning for ARES acquisition, significantly reducing measurement efficiency [35].

In this work, a novel angle-resolved ellipsometry (ARE) method is developed for SSD evaluation. First, limitations of q-BAT are addressed using EMA, and a new Ψ-ARES-based indicator, S_B, is proposed for SSD thickness quantification. Second, the enhanced q-BAT method is validated through FDTD simulations under oblique incidence, and a quantitative mapping function between SSD and S_B is established. Third, an ARE system is developed and applied to evaluate SSA in CaF_2 crystals, under varying polishing conditions. Validation experiments using WLI and TEM confirm the accuracy of the proposed method. This work highlights the potential of ARE as a powerful tool for nondestructive SSD evaluation, advancing surface quality inspection techniques.

2. Method

2.1. Principle of q-BAT

Ellipsometry characterizes a sample by measuring the changes in the polarization state of incident light upon reflection. The polarization state is typically expressed as the ratio of the wave component parallel (*p*-polarized) and perpendicular (*s*-polarized) to the plane of incidence. This ratio is represented using two parameters: the amplitude ratio Ψ and their phase retardance Δ, defined as:

$$\tan\Psi \cdot \exp(i\Delta) = r_p / r_s \tag{1}$$

where r_p and r_s are the Fresnel reflection coefficients for *p*- and *s*-polarized light, respectively. The Brewster angle (θ_B) is the incidence angle at which the reflected amplitude of *p*-polarized light vanishes [36], causing Ψ to reach its minimum value (zero for ideal surfaces). In contrast, the quasi-Brewster angle (θ_q) is the incidence angle where $\Delta = 90^{\circ}$ [29]. As illustrated in Fig. 1(a), q-BAT enables surface quality evaluation based on the following principles:

1) SSD layer thickness determines the angular shift, S_q, of the Δ-ARES curve at θ_q;
2) SR layer thickness influences the local gradient angle, G_q, of the Δ-ARES curve at θ_q.

The theoretical foundation of q-BAT lies in the EMA theory [37], which models SR or SSD as homogeneous materials with effective optical refractive indices. EMA provides a link between layer

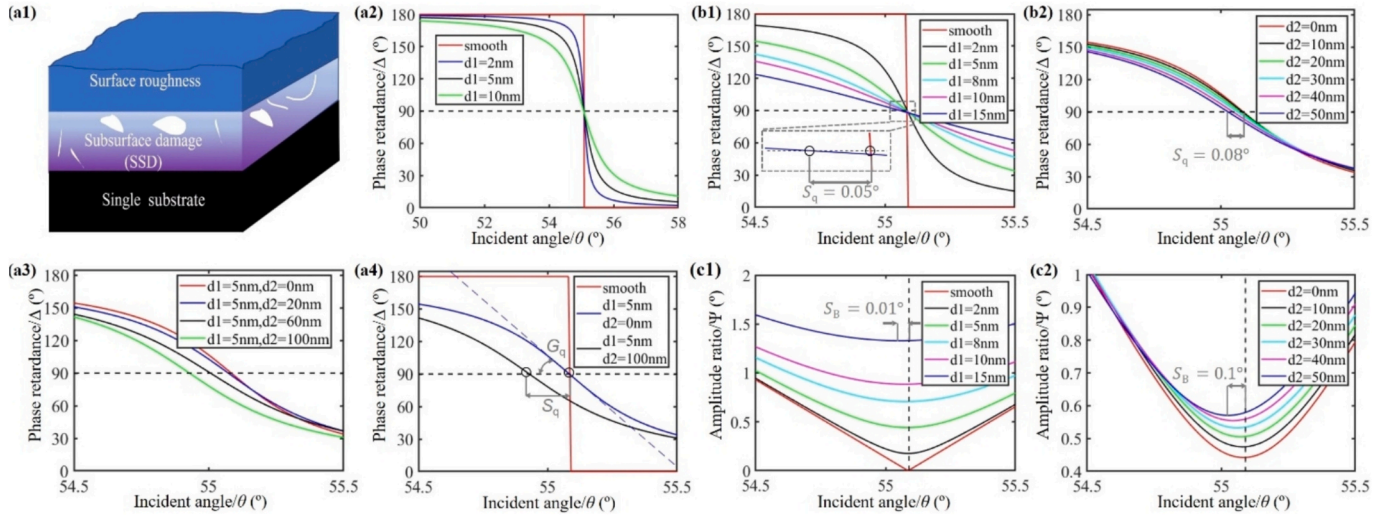

Fig. 1. EMA analysis of ARES regarding the variation of SR and SSD. (a1) Illustration of SR and SSD; (a2-a3) effect of SR and SSD on Δ-ARES, respectively; (a4) G_q and S_q on Δ-ARES derived from a combined effect of SR and SSD; (b1-b2) sensitivity of S_q to SR and SSD derived from Δ-ARES; (c1-c2) sensitivity of S_B to SR and SSD derived from Ψ-ARES. d_1 and d_2 represent SR and SSD layer thicknesses, respectively. In (b2) and (c2), $d_1 = 5nm$. G_q, S_q, and S_B correspond to the gradient angle, angular shift of θ_q in Δ-ARES, and the angular shift of θ_B in Ψ-ARES, respectively.

characteristics, e.g., thickness and void percentage, and optical properties, e.g., refractive index (n), as described by:

$$f_a\frac{\varepsilon_a-\varepsilon}{\varepsilon_a-2\varepsilon}+1(-f_a)\frac{\varepsilon_b-\varepsilon}{\varepsilon_b-2\varepsilon}=0 \quad (2)$$

where $\varepsilon = n^2$ is the effective dielectric constant, ε_a and ε_b are the dielectric constants of materials a and b, and f_a is the volume fraction of material a. For SSD layers, f_a represents the fraction of defects, such as cracks and pores and others.

An EMA-based q-BAT simulation was performed using MATLAB. The refractive index of air was set to 1, and the probing light wavelength was 632.8 nm. The refractive index of the CaF_2 substrate was 1.433, modelled using the Sellmeier equation [38]. The SR and SSD layers were modelled with 50 % and 1 % volume fractions, respectively. Their thicknesses, denoted as d_1 (SR) and d_2 (SSD), were varied to observe their effects on Δ-ARES. Fig. 1(a2) indicates that increasing SR thickness reduces G_q in the Δ-ARES curve. Fig. 1(a3) indicates that with a fixed SR thickness of 5 nm (typical for ultra-precision polishing), increasing SSD thickness increases S_q magnitude. Therefore, as illustrated in Fig. 1(a4), q-BAT resolves SR and SSD thicknesses independently by analyzing G_q and S_q, respectively.

2.2. Ψ-ARES-enhanced q-BAT

Despite its utility, the general q-BAT method has limitations. For example, the simulation results in Fig. 1(b1) show that as the SR layer thickness increased to 15 nm, a S_q of 0.05° was also observed. This value is equivalent to the S_q (0.08°) caused by an SSD of 50 nm thick, as presented in Fig. 1(b2). Both SR and SSD layer thicknesses in these simulations are commonly encountered in ultra-precision polishing practices [26,39,40]. The overlapping S_q values demonstrate a coupling effect, where S_q correlates with both SR and SSD, making SSD evaluation based solely on S_q unreliable. Additionally, cooperative evaluation using both S_q and G_q is time-consuming and prone to errors.

To address these issues, we propose a modified q-BAT method based on EMA analysis. The enhanced method replaces Δ-ARES with Ψ-ARES for SSD evaluation, as shown in Fig. 1(c). Under the same surface conditions as above, i.e., SR varying from 0 to 15 nm and SSD varying from 0 to 50 nm, S_B (derived from Ψ-ARES) exhibits distinct behaviors:

1) Fig. 1(c1) indicates that S_B remains nearly constant (0.01°) as SR increases, indicating insensitivity to SR;
2) Fig. 1(c2) indicates that S_B increases significantly (up to 0.1°) as SSD increases, demonstrating high sensitivity to SSD.

These results establish Ψ-ARES-resulted S_B as a more effective indicator for SSD evaluation than S_q. Based on this finding, therefore, this study combines S_B for SSD evaluation and G_q for SSD assessment as shown in Table 1, providing a more reliable approach for surface quality evaluation.

2.3. FDTD simulation

FDTD simulations were conducted to verify the feasibility of using Ψ-ARES for evaluating crystal SSD under oblique incidence, as well as the conclusions above. To enable simulations at multiple incidence angles, the plane wave Bloch/periodic boundary conditions were replaced by Broadband Fixed Angle Source Technique (BFAST). BFAST also replaced the Bloch boundary conditions in the x and y directions. The refractive index of CaF_2 material was set to 1.433. The geometric model used in the FDTD simulation is illustrated in Fig. 2(a), with corresponding settings and parameters listed in Table 2.

Fig. 2(b) shows the FDTD results (dotted lines) compared with EMA results (solid lines). Both methods produced consistent results, with identical G_q and S_q values, validating the coupling phenomenon observed in Section 2.2. Specifically, S_q correlates equally with SSD and SR, making it insufficient to distinguish between them. Fig. 1(a) demonstrates that G_q correlates strongly with SR. To quantify this, Fig. 2(c)

Table 1
Indicators of modified q-BAT for surface quality characterization.

Symbol	Definition	Object of evaluation
θ_q	Quasi-Brewster angle, the incidence angle corresponding to $\Delta = 90^\circ$	
θ_B	Brewster angle, the incidence angle at the minimum of Ψ-ARES	
S_q	Angular shift of θ_q in Δ-ARES	SSD*
G_q	Gradient angle of θ_q in Δ-ARES	SR
S_B	Angular shift of θ_B in Ψ-ARES	SSD

*Due to the high sensitivity of S_q to SR, S_B found in the Ψ-ARES replaces S_q for SSD evaluation in our study.

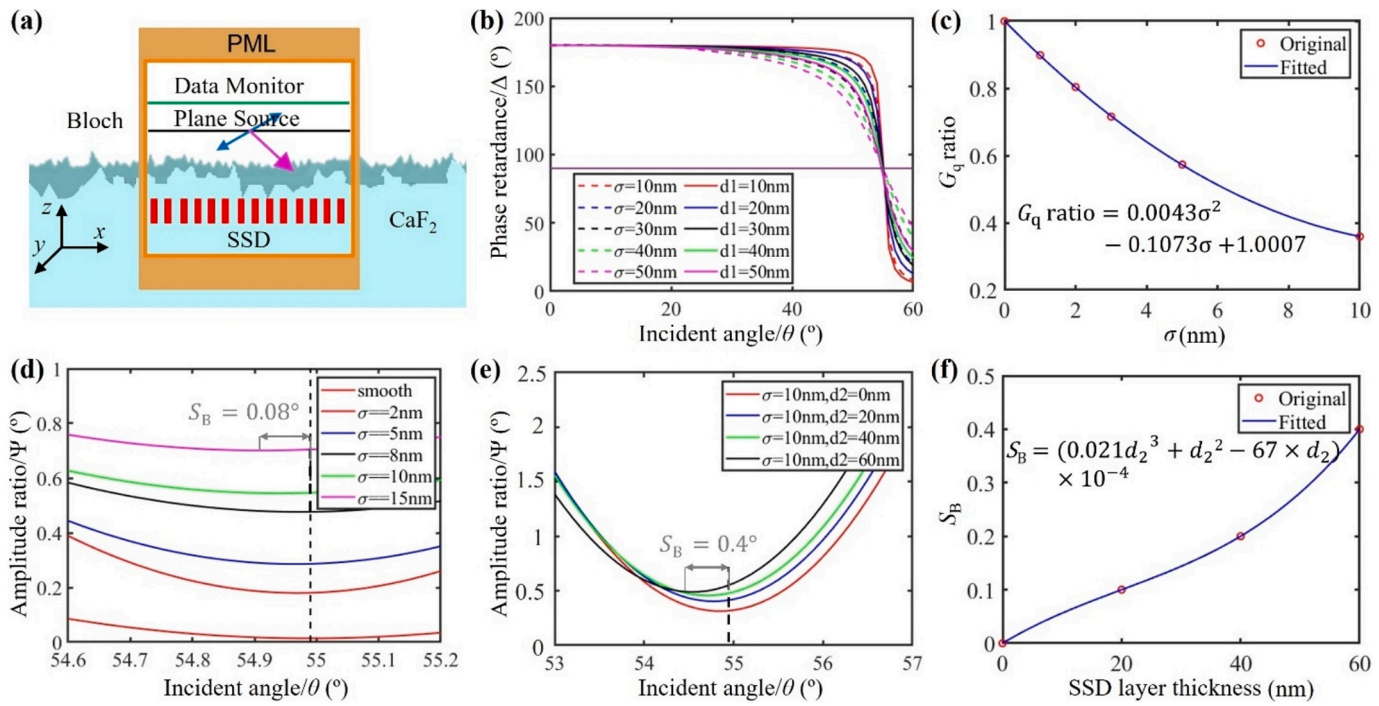

Fig. 2. FDTD simulation results. (a) FDTD geometric model with SR and SSD (red, enlarged for clarity); (b) effect of SR layer root-mean-square roughness σ on Δ-ARES obtained by FDTD (solid lines) compared to that of EMA (dashed lines); (c) functional mapping of G_q to SR·σ (G_q ratio relative to that of the ideal surface is calculated for practice convenience); (d, e) effect of SR and SSD on Ψ-ARES, respectively (zoomed 53° to 57° for clarity) for sensitivity analysis. (f) functional mapping of S_B to SSD thickness d_2 (S_B relative to that of the ideal surface with SR $\sigma = 10nm$·is calculated for convenience).

Table 2
Parameter settings of FDTD simulations.

	Parameter	Value
Boundary	*x*, *y* direction	BFAST
	z direction	PML
Probing Light	Type	BFAST
	Wavelength	632.8 nm
	Polarization angle	0 or 90°
	Angle phi	0°
	Amplitude	1
	Phase	0
Monitor	Type	Frequency domain field profile
SR Layer	Side lengthσ	1.5 μm
		2–50 nm
SSD Layer	Side length	10 nm
	Height	0–60 nm
	Number of rectangle void	10
	Pitch	10 nm
Substrate	Side length	3 μm

plots G_q as a function of root-mean-square SR (σ), showing a quadratic relationship that allows for the quantitative evaluation of SR using G_q.

Fig. 2(b) shows the FDTD results (dotted lines) compared with EMA results (solid lines). Both methods produced consistent results, with identical G_q and S_q values, validating the coupling phenomenon observed in Section 2.2. Specifically, S_q correlates equally with SSD and SR, making it insufficient to distinguish between them. Fig. 1(a) demonstrates that G_q correlates strongly with SR. To quantify this, Fig. 2(c) plots G_q as a function of root-mean-square SR (σ), showing a quadratic relationship that allows for the quantitative evaluation of SR using G_q.

The incidence angle range of 53 to 57° with a spacing of 0.1° was selected to optimize the simulation precision and efficiency. A quadratic polynomial was used for the local fitting of Ψ-ARES (54.6°-55.2°) to assess the impact of SSD layer thickness.

Regarding SR sensitivity, Fig. 2(d) shows the influence of SR layer thickness on Ψ-ARES. For σ ranging from 2 nm to 15 nm (consistent with Fig. 1(c1)), S_B remains nearly constant (0.08°), confirming that S_B is insensitive to SR, as concluded in Fig. 1(c1).

Regarding SSD sensitivity, an array of rectangular void structures representing SSD ("etch" in FDTD with a refractive index of 1) was added below the geometric model's rough surface, as presented in Fig. 2 (a). The SSD layer thickness was varied from 0 to 60 nm (0 represents no SSD). Fig. 2(e) illustrates that S_B increases significantly with SSD layer thickness ($S_B = 0.4^{\circ}$ for a 60 nm SSD layer), consistent with the results in Fig. 1(c2).

Fig. 2(f) plots the SSD layer thickness (0–60 nm) against S_B, where $\sigma = 10nm$. A quadratic relationship between SSD thickness and S_B is observed, enabling the quantitative evaluation of SSD. Similarly, Fig. 2 (c) demonstrates a quadratic relationship between SR and G_q, confirming the potential of G_q and S_B for separate evaluations of SR and SSD.

The FDTD simulation results confirm the feasibility of Ψ-ARES for evaluating SSD under oblique incidence conditions. Key findings include:

1) SR and SSD layer thicknesses can be independently evaluated using G_q and S_B (rather than S_q), respectively, obtained from Δ- and Ψ-ARES;
2) Quantitative mapping functions were established, including G_q for SR evaluation as a function of σ and S_B for SSD evaluation as a function of SSD layer thickness.

2.4. Principle of ARE

Variable angle spectroscopic ellipsometry (VASE) has traditionally been used to acquire ARES for SSD evaluation [30,31]. However, VASE measurements are inherently time-consuming, requiring typically 2–10 min per ARES acquisition [30], which significantly limits its use to off-line metrology. To overcome this limitation, building upon other reported works [41–45], we propose a new and effective ARES measurement method. ARE [35,46] captures polarized angle-resolved images through a high-NA (numerical aperture) objective lens's back-focal

plane (BFP), allowing ARES to be extracted from a single or a few images with polarization modulation.

The principle of ARE is illustrated in Fig. 3. An ARE system consists of three main parts: an illuminating light source, a measuring probe, and a detection unit. A white light source is collimated and passed through a narrow-band filter and a polarizer to generate monochromatic, polarized light. The beam is directed via a beam splitter and focused onto the sample surface through a high-NA objective lens. The *s*- and *p*-polarized components of the illuminating light vary with azimuthal angles across the sample surface. Reflected light from different incident angles is spatially resolved and focused at distinct points on the Fourier pupil plane. After modulation through another polarizer, the reflected light field at the BFP is captured by a 2D detector. Azimuthal polarization modulation enables the efficient extraction of ellipsometric parameter spectra from the BFP intensity image.

The relationship between the BFP radius and the incidence angle is depicted in Fig. 3(b). The radius corresponds to the NA of the objective lens, ranging from $-\sin^{-1}(\mathrm{NA})$ to $\sin^{-1}(\mathrm{NA})$. The relationship between the output electromagnetic wave amplitude E_{out} and the input wave amplitude is expressed as:

$$E_{out} = R_A(-A)J_A R_A(A)R(-\varphi)J_M J_S(\theta)R(\varphi) \times R_P(-P)J_P R_P(P)E_{in} \tag{3}$$

where J_P, J_S, J_A, and J_M are the Jones martices of the polarizer, sample, analyzer and redirected reflection, respectively; R is the rotation matrix, P and A represent the angle of the polarizer and analyzer; and φ is the azimuthal angle. If $A = \pi/4$ and $P = 0$, the BFP output intensity $I_{\mathrm{out}} = E_{\mathrm{out}} \cdot E^*_{\mathrm{out}}$, has the following form:

$$I_{out}(\theta,\varphi) = \alpha_0(\theta) + \alpha_1(\theta)\sin\left(2\varphi + \frac{\pi}{4}\right) + \alpha_2(\theta)\sin(4\varphi) \tag{4}$$

which is a function of incident angle θ and azimuthal angle φ. Harmonic coefficients α_0, α_1 and α_2 are extracted using digital phase-shifting [46] from a single-shot BFP image. Ψ- and Δ-ARES for each incident angle are calculated as:

$$\tan^2\Psi(\theta) = \frac{\sqrt{2}\alpha_0(\theta) + \alpha_1(\theta)}{-\sqrt{2}\alpha_0(\theta) + \alpha_1(\theta)} \tag{5}$$

$$\cos(\theta) = \frac{(2\alpha_2(\theta) - \alpha_0(\theta))(\tan^2\Psi(\theta+1))}{2\alpha_2(\theta)\tan\Psi(\theta)} \tag{6}$$

3. Results and discussion

3.1. Experimental setup

A set of ultra-precision polished CaF_2 crystals (Shanghai Puruiduo Optical Materials Co., China) were used as "ideal" samples. These samples have a diameter of 30 mm and a thickness of 2 mm. The SR of the ideal sample was measured using an atomic force microscope (AFM, Bruker Dimension Icon), as shown in Fig. 5(a) and (e). The samples were sequentially ground and then polished using a BUEHLER EcoMet 250 system to generate SSD with varying severities, as shown in Fig. 4(a). The processing parameters for SSD artefact preparation are summarized in Table 3. To meet the polishing requirements, the bottom surfaces of the CaF_2 crystals were embedded in resin before processing.

Samples were cleaned using an ultrasonic cleaning machine with deionized water and ethanol and then dried with pure nitrogen gas for SSD inspection. An ARE system was developed to evaluate the surface quality of the samples, as shown in Fig. 4(b). WLI and TEM were used to characterize SR and SSD of the samples, respectively, to validate the accuracy of the ARE method. The diameter of the measured light spot was 54.91 μm. The measurement time is directly affected by the exposure time, in this paper, the time required for a single measurement is 50 ms. Focused ion beam (FIB) technique was used to prepare cross-sectional samples for TEM observations.

3.2. Results of AFM, WLI and TEM

Typical samples were selected for SR measurement using a Zygo NewView 6000, a powerful WLI. The effect of the polishing process on SR was investigated by observing samples at three stages: the initial stage of rough polishing (R20), the final stage of rough polishing (R70), and the final stage of fine polishing (F30). SR measurements were performed on randomly selected areas (three repetitions) for each sample using a 20X objective lens. Surface topography portions with 850 μm and 120 μm side lengths were obtained.

Fig. 5 presents the WLI surface topography results with local magnification.

1) After 20 min of rough polishing, surface defects such as holes and cracks were observed, indicating significant surface irregularities.

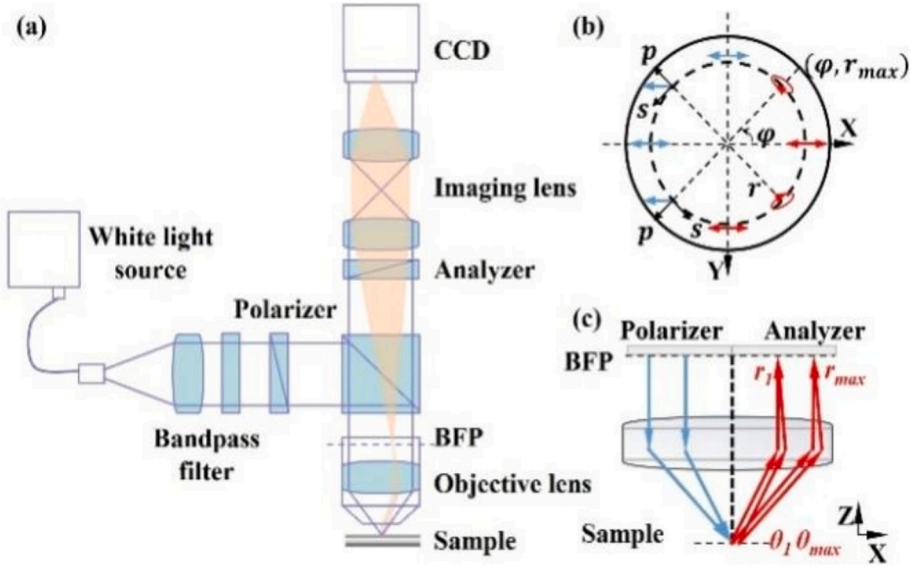

Fig. 3. Principle of ARE measurement. (a) Optical configuration, (b) polarization status on the BFP pupil, and (c) the relationship between the BFP radius (r) and incident angle (θ). Incident and reflected beams are noted in blue and red, respectively.

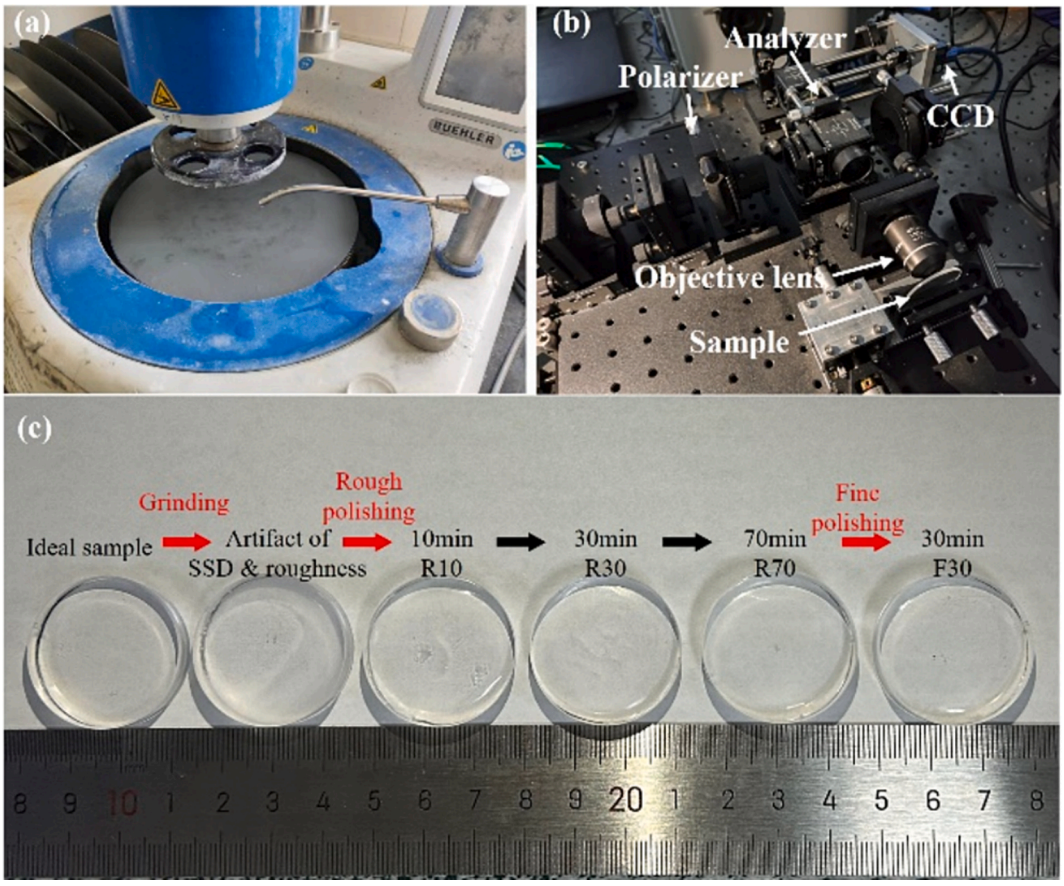

Fig. 4. Experimental equipment and materials. (a) Polishing machine, (b) ARE system, and (c) typical processed samples. R and F represent the rough and fine polishing stages, respectively.

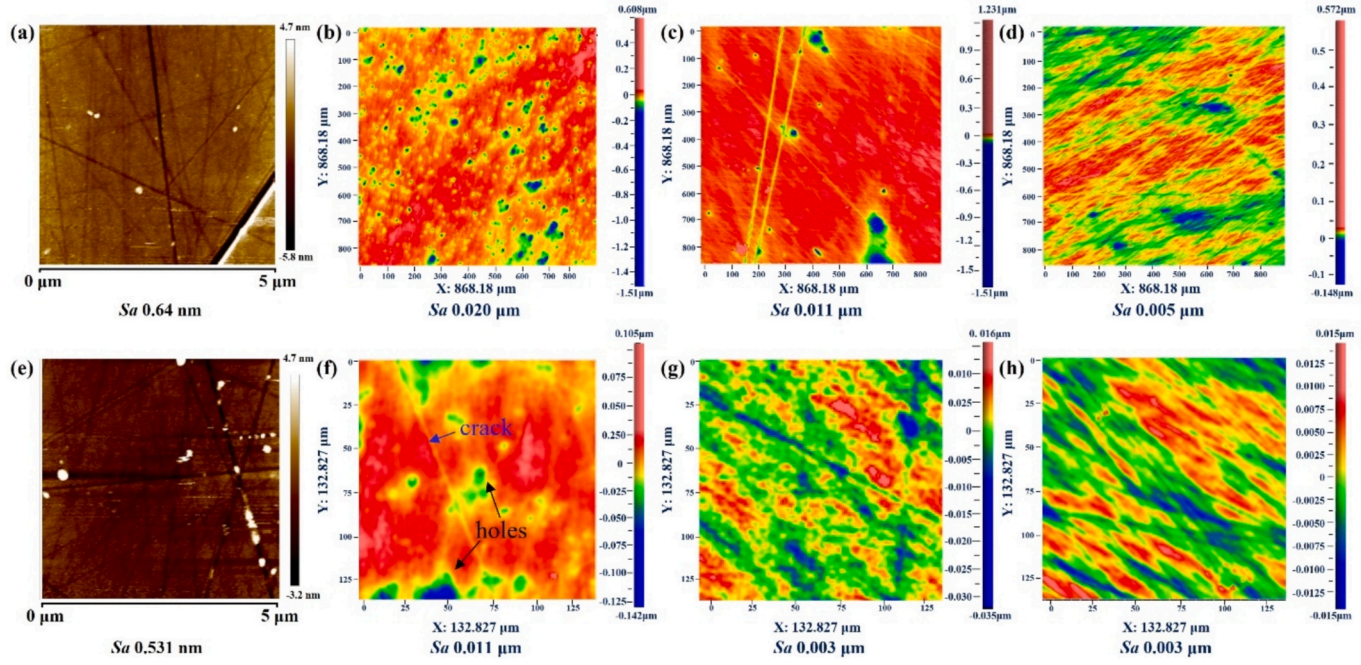

Fig. 5. AFM and WLI measurement results of CaF_2 samples. (a, e) Surface topography of "ideal" sample; (b-d) surface topography of R20, R70, F30 and their local zooms (f-h), with a mean *Sa* of 0.5 nm, 10.6 nm, 3.4 nm and 2.6 nm, respectively.

Table 3
Processing parameters of SR-SSD artifacts through grinding and polishing.

Sample	Process	Material	Parameter	Duration
SR/SSD Artifact	Rough grinding	Grinding disc: W40 Cast iron plate	Polishing speed: 50r /min Grinding disc speed: 50 r/ min Grinding load: 5 N/cm^2	4 min
	Fine grinding	Grinding disc: W20 Cast iron plate	Polishing speed: 50 r/ min Grinding disc speed: 60 r/ min Grinding load: 5 N/cm^2	12 min
R10 R20 R30 R50 R70	Rough polishing	Polishing disc: IC 1000 polyurethane plate Polishing solution: W2.5 Al_2O_3	Polishing speed: 50 r/ min Polishing disc speed: 70 r/ min Polishing load: 5 N/cm^2	10 min 20 min 30 min 50 min 70 min
F10 F30	Fine polishing	Polishing disc: IC 1000 polyurethane plate Polishing solution: W0.1 SiO_2	Polishing speed: 50 r/ min Polishing disc speed: 70 r/ min Polishing load: 5 N/cm^2	10 min 30 min

2) After 70 min of rough polishing, surface pits decrease dramatically, leaving nanoscale scratches visible, as shown in Fig. 5(c, g);
3) After 30 min of fine polishing, surface defects were nearly eliminated, and the average SR, *Sa*, decreased to 2.6 nm, as shown in Fig. 5(d, h).

These results demonstrate that fine polishing can produce a surface suitable for next-generation atomic-level ultraprecision manufacturing.

Fig. 6 shows the cross-sectional TEM (FEI Tecnai G2 20) images of sample F30 at different resolutions. Pt and Au layers were sputtered on sample surfaces to prevent FIB damage and enhance conductivity. The results show that the SSD layer thickness is approximately 20 nm, with an amorphous layer thickness of ~10 nm. Lattice dislocations were found below the layer. These observations are consistent with previous studies [30], which reported the formation of amorphous layers during conventional grinding and polishing. Optimized processing methods, such as plasma treatment with chemical mechanical polishing [47], inductively coupled plasma [48], and plasma-assisted polishing [49], have been developed to produce SSD-free polished crystals.

3.3. Results of ARE

Fig. 7 presents the ARES of Ψ and Δ obtained from the CaF_2 samples using the proposed ARE system. Ten randomly selected surface portions of each sample were measured and averaged to ensure reproducibility. Fig. 7(e) shows the ten original Ψ-ARES curves of sample R70. During the evaluation of SR and SSD, a fifth-order polynomial was used to fit the ten raw spectra (within the range of 40-60°) for noise suppression, as demonstrated in Fig. 7(a) and (d). Fig. 7(a) shows that the mean Δ-ARES of the treated samples gradually approached the ideal sample along with the progression of the polishing process.

Fig. 7(b) and (c) present the variations of S_q and the G_q ratio during different processing stages based on Δ-ARES analysis. Key findings include:

1) During early polishing (R10-R20), S_q and G_q (ratio over that of the ideal sample was analyzed) increased due to the exposure of damages caused by grinding of the SSD artefacts. This phenomenon aligns with previous findings by Chu et al. [15], who observed similar non-monotonic SR variations using chemical etching.
2) After extended polishing (R50-R70), G_q and S_q returned gradually to a constant after 50 min of rough polishing, indicating the achievement of a stable surface quality.
3) After final polishing (F10-F30), G_q indicated that SR approached about 2 nm, consistent with the WLI results. This correlation demonstrates the validity of G_q for SR evaluation, even though G_q was derived through FDTD simulations without considering SSD presence.

However, the TEM results revealed that the subsurface contained an amorphous layer and lattice dislocations. This contradicts S_q, which converged to that of the initial "ideal" sample, confirming that S_q alone is unreliable for SSD characterization (consistent with the conclusion from the EMA study in Fig. 1(b)).

The Ψ-ARES method was employed for SSD evaluation, as shown in Fig. 7(d). As the polishing process progressed, the Ψ-ARES spectra increasingly resembled those of the ideal sample. The following key insights are resulted from Fig. 7(f):

1) During early polishing (R10-R20), S_B remained unchanged between R10 and R20, indicating that the polishing had not removed SSD.
2) After extended polishing (R50-R70), S_B approaches the ideal sample, but a larger STD indicates a non-uniform SSD removed.

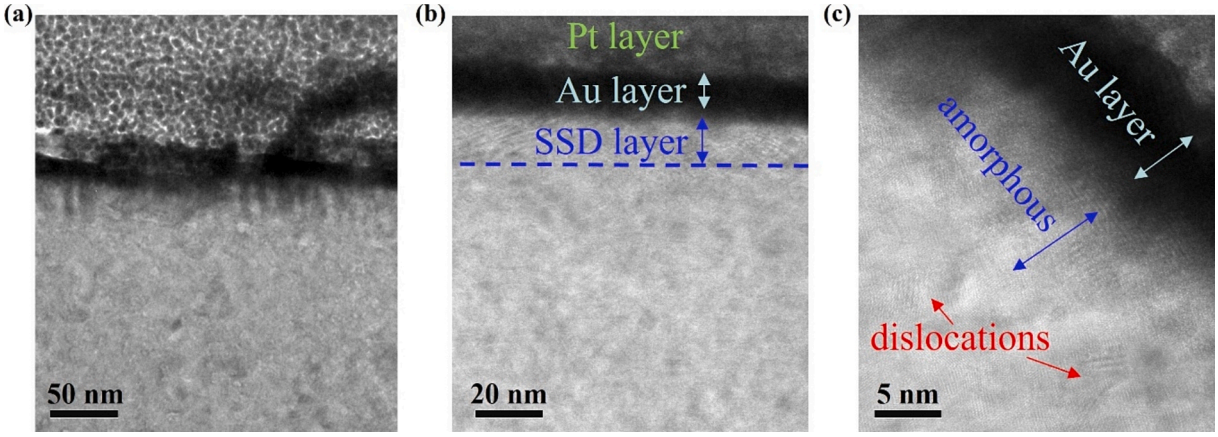

Fig. 6. TEM images of SSD of sample F30 with different resolutions.

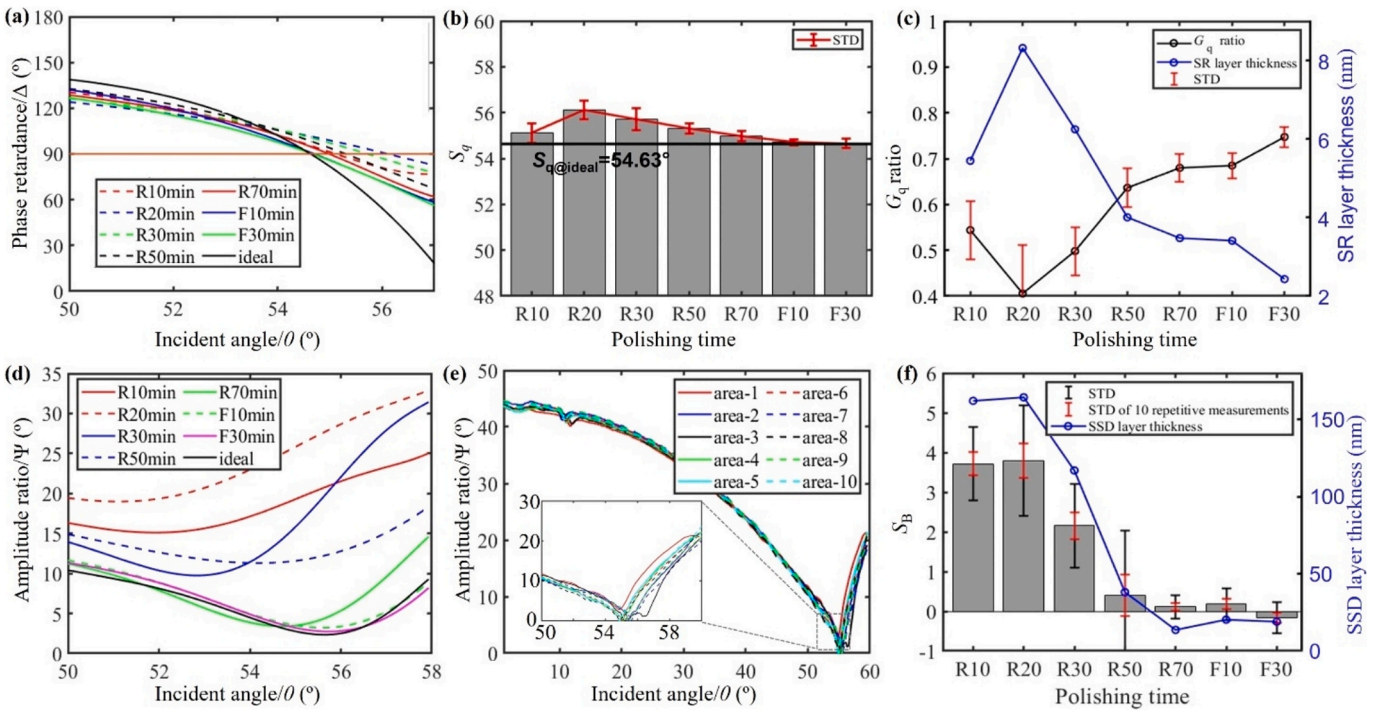

Fig. 7. ARES analysis for SR and SSD evaluation of CaF_2 samples under various processing conditions. (a) Zoomed view of fitted Δ-ARES and corresponding S_q (b) and G_q for SR evaluation (c), where G_q ratio over that of the ideal sample is analyzed for convenience (same in Fig. 2c), and the error bars represent the STD of 10 measurement areas; (d)zoomed view of fitted Ψ-ARES and extracted S_B for SSD evaluation (f); (e) original and zoom view Ψ-ARES of ten repetitive measurements for sample R70.

3) After final polishing (F10-F30), S_B and STD stabilized to nearly match the ideal sample. Combined with G_q results in Fig. 7(c), this indicates the near-complete elimination of SSD.

The accuracy of the S_B method was validated by comparing SSD values derived from S_B at F30 with those from TEM images. In addition, Fig. 7(f) confirmed a slight improvement in subsurface quality due to the over-polishing process, consistent with the observations by Yao et al. [30]. These results demonstrate the feasibility of the S_B method for evaluating SSD and highlight the reliability of the ARE system for characterizing complex samples.

It should be noted that, at the initial stage of rough polishing, the STDs of S_B for SSD measurements were significant due to large SR and surface non-uniformity. However, repetitive measurements (10 repetitions in the study) ensured acceptable reliability. The single-shot nature of ARE technology facilitates such repeated measurements without compromising efficiency, further enhancing the robustness of the proposed method.

4. Conclusion

This study introduces a novel method for evaluating the surface quality of polished crystals using angle-resolved ellipsometry. Addressing the limitations of the current quasi-Brewster angle technique, we proposed a new approach based on angle-resolved ellipsometric spectra (ARES) of Ψ for distinguishing subsurface damage (SSD) from surface roughness (SR).

Through finite-difference time-domain simulations, we demonstrated the feasibility of Ψ-ARES under oblique incidence conditions, establishing quantitative relationships between SR layer thickness and gradient angle G_q, as well as SSD layer thickness and Brewster angle shift S_B, obtained from Δ- and Ψ-ARES, respectively. These insights provide a robust theoretical foundation for nondestructive SSD evaluation.

Experimental validation was conducted on CaF_2 crystal samples with varying polishing parameters. The measurement results obtained from a developed ARE system were validated using white light interferometry and transmission electron microscopy, confirming the reliability of the Ψ-ARES-enhanced q-BAT method. The results also highlighted the capability of Ψ-ARES to assess both SR and SSD independently, offering a significant advantage over existing methods.

This work demonstrates that the Ψ-ARES-enhanced q-BAT method, integrated with snapshot ARE, provides a rapid, nondestructive, and highly accurate tool for surface quality evaluation. Though CaF_2crystals are demonstrated only in the study, its application extends beyond polished to other materials in ultra-precision machining, making it a promising technology for advancing quality control and metrology in manufacturing processes.

CRediT authorship contribution statement

Tianqi Jia: Writing – original draft, Methodology, Investigation, Data curation. **Jian Wang:** Writing – review & editing, Validation, Supervision. **Lihua Peng:** Writing – review & editing, Writing – original draft, Methodology. **Wei Guo:** Writing – review & editing, Validation. **Wenjuan Sun:** Writing – review & editing, Validation. **Shiyuan Liu:** Writing – review & editing, Supervision.

Declaration of competing interest

The authors declare that they have no known competing financial interests or personal relationships that could have appeared to influence the work reported in this paper.

Acknowledgments

This work was supported by National Natural Science Foundation of China (52475557), Huazhong University of Science and Technology (5019190003), National Key Research and Development Program (2023YFB4606000) and Innovation Project of Optics Valley Laboratory (OVL2023PY003).

Data availability

Data will be made available on request.

References

[1] N.J. Guo, G.S. Zhu, H.R. Xu, X.P. Jiang, X.Y. Zhang, J.J. Song, Y.Y. Zhao, et al., Preparation of CaF2 transparent ceramics by cold sintering, Ceram. Int. 48 (23) (2022) 34184–34189.

[2] X. Li, X.A. Dou, H. Zhu, Y. Hu, X. Wang, et al., Nanosecond laser-induced surface damage and its mechanism of CaF2 optical window at 248nm KrF excimer laser, Sci. Rep. 10 (2020) 5550.

[3] J.X. Gong, C. Yu, J.X. Peng, Y.B.J. PengJF, L. Chen, et al., Stress-enhanced dissolution and delamination wear of crystal CaF2 in water condition, Wear 418 (2019) 86–93.

[4] X. Chen, X. Yang, X. Xie, Y. Peng, L.F. Xiao, C. Shao, et al., Research progress of large size SiC single crystal materials and devices, Light-Sci. Appl. 12 (1) (2023) 28.

[5] M. Xu, B. Liu, L. Zhang, H.K. Ren, Q.T. Gu, X. Sun, et al., Progress on deuterated potassium dihydrogen phosphate (DKDP) crystals for high power laser system application, Light-Sci. Appl. 11 (1) (2024) 241.

[6] X.Y. Chen, Y. Gu, J.Q. Lin, A. Yi, M.S. Kang, X.Y. Cang, Study on subsurface damage and surface quality of silicon carbide ceramic induced by a novel non-resonant vibration-assisted roll-type polishing, J. Mater. Process. Tech. 282 (2020) 116667.

[7] A.R. Alao, Review of ductile machining and ductile-brittle transition characterization mechanisms in precision/ultraprecision turning, milling and grinding of brittle materials, Precis. Eng. 88 (2024) 279–299.

[8] W.Y. Ding, L.J. Zhao, M.J. Chen, J. Cheng, Z.Y. Yin, Q. Liu, G. Chen, et al., Concentration characterization of underlying intrinsic defects accompany with surface structural defects and their effect on laser damage resistance, Appl. Surf. Sci. 643 (2024) 158678.

[9] W. Li, X.L. Hu, Y.H. Ren, S.L. Zhou, C. Mao, Y.T. Zhou, A.M.M. Ibrahim, Ultra-precision lapping of H2O(g) plasma-treated CaF2 by porous diamond grits, Ceram. Int. 50 (5) (2024) 7281–7292.

[10] Q. Luo, J. Lu, Z. Tian, F. Jiang, Controllable material removal behavior of 6H-SiC wafer in nanoscale polishing, Appl. Surf. Sci. 562 (34) (2021) 150219.

[11] W. Liao, Y. Dai, X. Xie, L. Zhou, Microscopic morphology evolution during ion beam smoothing of Zerodur® surfaces, Opt. Express 22 (1) (2014) 377–386.

[12] C. Li, Y.C. Piao, B.B. Meng, Y.X. Hu, L.Q. Li, F.H. Zhang, Phase transition and plastic deformation mechanisms induced by self-rotating grinding of GaN single crystals, Int. J. Mach. Tools Manuf. 172 (2022) 103827.

[13] Y. Zhang, Q.C. Fan, W. Gao, C. Wang, F. Ji, Subsurface damage layer of bulk single-crystal potassium dihydrogen phosphate (KDP) after SPDT: Studied by the grazing incidence X-ray diffraction technique, Opt. Mater. Express 12 (5) (2022) 2041–2052.

[14] H.P. Xiao, F. Zhang, S.X. Yin, C.F. Cheung, C.J. Wang, Subsurface damage model in single and double scratching of fused silica with a blunt indenter, Int. J. Mech. Sci. 250 (2023) 108309.

[15] J.N. Chu, X. Liu, C.L. Liu, J.G. Zhang, J.F. Xiao, X.F. Wang, et al., Fundamental investigation of subsurface damage on the quality factor of hemispherical fused silica shell resonator, Sensor Actuat. A-Phys. 335 (2022) 113365.

[16] Y.F. Guo, Y.J. Lee, Y. Zhang, A. Sorkin, S. Manzhos, H. Wang, Effect of a weak magnetic field on ductile-brittle transition in micro-cutting of single-crystal calcium fluoride, J. Mater. Sci. Technol. 112 (2022) 96–113.

[17] H.F. Tao, Q.Y. Zeng, Y.H. Liu, D.W. Zhao, X.C. Lu, Influence of anisotropy on material removal and deformation mechanism based on nanoscratch tests of monocrystal silicon, Tribol. Int. 187 (2023) 108736.

[18] K. Wei, C.K. Lin, P.C. Tung, J.R. Ho, I.Y. Tsao, Formation of subsurface Cu-O-Si system through laser-induced plasma-assisted copper penetration for fabricating robust adhesive copper wire on glass substrate, Appl. Surf. Sci. 609 (2023) 155149.

[19] M.Q. Liu, J.H. Wang, W. Liu, H.J. Wu, J.L. Yuan, B. Lyu, G.J. Peng, et al., Force rheological polishing of polycrystalline magnesium aluminate spinel using agglomerated diamond abrasive, Ceram. Int. 50 (24) (2024) 55275–55285.

[20] S. Frank, M. Seiler, J. Bliedtner, Three-dimensional evaluation of subsurface damage in optical glasses with ground and polished surfaces using FF-OCT, Appl. Opt. 60 (8) (2021) 2118–2126.

[21] Y.V. Korkh, A.M. Burkhanov, A.B. Rinkevich, Scanning acoustic microscope for visualization of microflaws in solids, Russ. J. Nondestruct. 45 (10) (2009) 677–684.

[22] H. Yu, Scanning acoustic microscopy for material evaluation, Appl. Micro. 50 (1) (2020) 25.

[23] J.R. Zhang, S.W. Lu, G.F. Shi, W.K. Xie, W.ZB. GengYQ, A study on a hybrid SERS substrates based on arrayed gold nanoparticle/graphene/Copper cone cavities fabricated by a conical tip indentation, J. Mater. Res. Technol. 22 (2022) 1558–1571.

[24] J.R. Zhang, J.S. Wu, B.H. Wang, Y.Q. Geng, Z.B. Wang, A new strategy for constructing 3D hybrid graphene/Au/rectangular pyramids PMMA on a flexible SERS substrate for trace molecule detection, Sensor Actuat. B-Chem. 410 (2024) 135711.

[25] Z.W. Xu, Z.D. He, Y. Song, X. Fu, M. Rommel, X.C. Luo, et al., Topic review: Application of Raman spectroscopy characterization in micro/nano-machining, Micromachines 9 (7) (2018) 361.

[26] H.C. Zhou, J. Gao, H.L. Zhang, J. Zhu, L.M. Qian, B.J. Yu, Mechanochemical removal of lithium aluminosilicate glass-ceramics, Tribol. Int. 186 (2023) 108629.

[27] N. Hayazawa, M. Motohashi, Y. Saito, A. Ono, T. Ichimura, P. Verma, et al., Visualization of localized strain of a crystalline thin layer at the nanoscale by tip-enhanced Raman spectroscopy and microscopy, J. Raman Spectrosc. 38 (6) (2007) 684–696.

[28] Y. Zhang, Q. Wang, C. Li, Y.C. Piao, N. Hou, K.N. Hu, Characterization of surface and subsurface defects induced by abrasive machining of optical crystals using grazing incidence X-ray diffraction and molecular dynamics, J. Adv. Res. 36 (2021) 51–61.

[29] J. Wang, R.L. Maier, Quasi-Brewster angle technique for evaluating the quality of optical surfaces, Proc. SPIE 5375 (2004) 1286–1294.

[30] C.Y. Yao, W.F. Shen, X.D. Hu, C.G. Hu, Evaluation of the surface and subsurface evolution of single-crystal yttrium aluminum garnet during polishing, Appl. Surf. Sci. 608 (2023) 155219.

[31] C.Y. Yao, W.F. Shen, X.D. Hu, C.G. Hu, Surface and subsurface quality assessment of polished Lu2O3 single crystal using Quasi-Brewster angle technique, Front. Phys. 9 (2021) 795639.

[32] W.P. Yu, C.C. Cui, H.H. Li, S.B. Bian, X. Chen, FDTD-based study on equivalent medium approximation model of surface roughness for thin films characterization using spectroscopic ellipsometry, Photonics 9 (9) (2022) 621.

[33] M.J. Huang, L. Guo, F.Y. Jiang, Regime map of the effective medium approximation modelling of micro-rough surfaces in ellipsometry, Sensors 24 (4) (2024) 1242.

[34] T.H. Fung, T. Veeken, D. Payne, B. Veettil, A. Polman, M. Abbott, Application and validity of the effective medium approximation to the optical properties of nano-textured silicon coated with a dielectric layer, Opt. Express 27 (26) (2019) 38645–38660.

[35] G. Choi, S.W. Lee, H.J. Pahk, S.W. Lee, I.N. Shin, C.H. Yoon, et al., Single-shot multi-spectral angle-resolved ellipsometry, Appl. Opt. 59 (21) (2020) 6296–6303.

[36] K.V. Sreekanth, M. Elkabbash, R. Medwal, J.H. Zhang, T. Letsou, G. Strangi, et al., Generalized Brewster-angle effect in thin-film optical absorbers and its application for graphene hydrogen sensing, ACS Photonics 6 (7) (2019) 1610–1617.

[37] D. Bruggeman, Calculation of various physics constants in heterogenous substances I Dielectricity constants and conductivity of mixed bodies from isotropic substances, Annalen der Physik 4 (1935) 636.

[38] Q.F. Zheng, X.C. Wang, D. Thompson, Temperature-dependent optical properties of monocrystalline CaF2, BaF2, and MgF2, Opt. Mater. Express 13 (8) (2023) 2380–2391.

[39] Y.J. Guo, X.J. Yang, J. Kang, W.Q. Zhang, X.Y. Wang, M.Z. Li, Y.K. Wang, et al., Ductile machining of single-crystal germanium for freeform surfaces diamond turning based on a long-stroke fast tool servo, J. Manuf. Process. 82 (2022) 615–627.

[40] H.F. Tao, Y.H. Liu, C.X. Wang, D.W. Zhao, X.C. Lu, Cutting speed dependence of material removal mechanism for monocrystal silicon, Int. J. Mech. Sci. 264 (2024) 108816.

[41] P. Petrik, N. Kumar, M. Fried, B. Fodo, G. Juhasz, S.F. Pereira, et al., Fourier Ellipsometry – an ellipsometric approach to fourier scatterometry, J. Eur. Opt. Soc.-Rapid. 10 (2015) 15002.

[42] N. Kumar, P. Petrik, G.K.P. Ramanandan, O. Gawhary, S. Roy, S.F. Pereira, et al., Reconstruction of sub-wavelength features and nano-positioning of gratings using coherent Fourier scatterometry, Opt. Express 22 (20) (2014) 24678–24688.

[43] P. Boher, R.M. Silver, J. Petit, T. Leroux, J. Foucher, Y. Desieres, et al., Optical Fourier transform scatterometry for LER and LWR metrology, SPIE 5752 (2005) 192.

[44] L.H. Peng, J. Wang, F. Gao, J. Zhang, W.Z. Zhai, L.P. Zhou, X.Q. Jiang, Incoherent partial superposition modeling for single-shot angle-resolved ellipsometry measurement of thin films on transparent substrates, Opt. Express 32 (9) (2024) 15774–15787.

[45] J. Wang, L.H. Peng, F.Q. Zhai, D.W. Tang, F. Gao, X.C. Zhang, R. Chen, et al., Polarized angle-resolved spectral reflectometry for real-time ultra-thin film measurement, Opt. Express 31 (4) (2023) 6552–6565.

[46] L.H. Peng, D.W. Tang, J. Wang, R. Chen, F. Gao, L.P. Zhou, Robust incident angle calibration of angle-resolved ellipsometry for thin film measurement, Appl. Opt. 60 (13) (2021) 3971–3976.

[47] Z.H. Kou, C. Wang, W.J. Zhou, A.L. Chen, Y. Chen, Trivalent lanthanum and ytterbium doped meso-silica/ceria abrasive systems toward chemical mechanical polishing (CMP) and ultraviolet irradiation-assisted photochemical mechanical polishing (PCMP), Appl. Surf. Sci. 657 (2024) 159733.

[48] Q.B. Li, S.Z. Wang, L. Liu, K.P. Song, J.X. Yu, G.D. Wang, J.L. Liu, et al., Efficient access to non-damaging GaN (0001) by inductively coupled plasma etching and chemical–mechanical polishing, Appl. Surf. Sci. 679 (2025) 161207.

[49] N. Liu, K. Sugimoto, N. Yoshitaka, H. Yamada, R.Y. Sun, K. Arima, K. Yamamura, Highly efficient finishing of large-sized single crystal diamond substrates by combining nanosecond pulsed laser trimming and plasma-assisted polishing, Ceram. Int. 49 (11) (2023) 19109–19123.